*J Neurophysiol* 111: 533–543, 2014.
First published November 6, 2013; doi:10.1152/jn.00549.2013.

# Dynamics and cortical distribution of neural responses to 2D and 3D motion in human

**Benoit R. Cottereau,[1] Suzanne P. McKee,[2] and Anthony M. Norcia[3]**

[1]*Centre de Recherche Cerveau et Cognition, Centre National de la Recherche Scientifique CERCO UMR 5549, Toulouse, France;* [2]*The Smith-Kettlewell Eye Research Institute, San Francisco, California; and* [3]*Department of Psychology, Stanford University, Stanford, California*

Submitted 1 August 2013; accepted in final form 6 November 2013

**Cottereau BR, McKee SP, Norcia AM.** Dynamics and cortical distribution of neural responses to 2D and 3D motion in human. *J Neurophysiol* 111: 533–543, 2014. First published November 6, 2013; doi:10.1152/jn.00549.2013.—The perception of motion-in-depth is important for avoiding collisions and for the control of vergence eye-movements and other motor actions. Previous psychophysical studies have suggested that sensitivity to motion-in-depth has a lower temporal processing limit than the perception of lateral motion. The present study used functional MRI-informed EEG source-imaging to study the spatiotemporal properties of the responses to lateral motion and motion-in-depth in human visual cortex. Lateral motion and motion-in-depth displays comprised stimuli whose only difference was interocular phase: monocular oscillatory motion was either in-phase in the two eyes (lateral motion) or in antiphase (motion-in-depth). Spectral analysis was used to break the steady-state visually evoked potentials responses down into even and odd harmonic components within five functionally defined regions of interest: V1, V4, lateral occipital complex, V3A, and hMT+. We also characterized the responses within two anatomically defined regions: the inferior and superior parietal cortex. Even harmonic components dominated the evoked responses and were a factor of approximately two larger for lateral motion than motion-in-depth. These responses were slower for motion-in-depth and were largely independent of absolute disparity. In each of our regions of interest, responses at odd-harmonics were relatively small, but were larger for motion-in-depth than lateral motion, especially in parietal cortex, and depended on absolute disparity. Taken together, our results suggest a plausible neural basis for reduced psychophysical sensitivity to rapid motion-in-depth.

stereomotion; high-density EEG; vision; 3D

WHILE TWO-DIMENSIONAL (2D) motion processing has been widely investigated in the primate brain, the neural mechanisms associated with three-dimensional (3D) motion are less well understood. Forty years ago, Regan and Beverley (1973a, 1973b) used psychophysical measures to distinguish differences between lateral motion and motion-in-depth (MID). To isolate responses specific to the type of motion, they cleverly used a stimulus that was identical monocularly, a line oscillating continuously back and forth. Either the line moved in the same direction in both eyes, i.e., in phase, producing lateral motion, or in opposite directions between the two eyes, i.e., in antiphase, producing MID. Regan and Beverley's major finding was a difference in the temporal characteristics of the two types of motion; the ability to detect oscillations in depth essentially disappeared above 5 Hz, while oscillations in lateral motion were visible up to about 20 Hz. Later psychophysical studies (Nienborg et al. 2005; Norcia and Tyler 1984) have found that disparity modulation is distinguishable from disparity noise at much higher temporal frequencies than 5 Hz, but the defining characteristics of lateral motion, coherent direction and speed, are not apparent for MID at these high frequencies.

Surprisingly, the neural mechanisms responsible for the differences in the dynamics of lateral motion and MID have not been investigated in detail. Instead, most ensuing research on MID has focused on its computational basis. Beverley and Regan (1975) suggested that MID was based on the interocular velocities difference (IOVD) between the motions in the two eyes. However, based on their psychophysical studies, Cumming and Parker (1994) proposed that MID depended solely on the detection of changes in disparity over time (CDOT). Although these two models imply vastly different neural architectures (IOVD is based on motion-selective cells, while CDOT is based on disparity-selective cells), most current studies have shown that both IOVD and CDOT support the perception of MID (Nefs et al. 2010; Rokers et al. 2009). It should be noted that neither IOVD nor CDOT cues alone are sufficient for defining 3D motion trajectories in a general fashion (Lages and Heron 2010).

A recent study has shed new light on possible cortical origins of the differential temporal dynamics associated with lateral motion and MID. By combining single-cell recording and cooling in macaque, Ponce et al. (2008) provided compelling evidence that the V1 neural responses to disparity and those to motion travel via different pathways en route to area MT. The motion-related pathway is direct, while the disparity pathway is indirect and passes first through extrastriate areas V2 and V3. If we assume that some aspects of MID perception depend on disparity-selective cells, the slower responses observed for MID in Regan and Beverley (1973a, 1973b) could be explained by the integration of the disparity information along this indirect and therefore slower pathway.

The aim of this study is to compare the neural population responses to lateral motion and to MID in human observers. We used a high-density electroencephalogram (EEG) imaging technique, which, coupled to visual areas defined by functional magnetic resonance imaging (fMRI) (Cottereau et al. 2012a), allowed us to examine the cortical responses elicited by these two conditions within five distinct functional regions of interest (ROIs): V1, V4, lateral occipital complex (LOC), V3A, and hMT+. We were specifically interested in their temporal characteristics and in their functional connectivity. In rough imitation of the Regan-Beverley stimulus configuration, we

Address for reprint requests and other correspondence: B. R. Cottereau, CNRS CERCO UMR 5549, Pavillon Baudot CHU Purpan, BP 25202, 31052 Toulouse Cedex, France (e-mail: cottereau@cerco.ups-tlse.fr).

used moving random dot stimuli that differed only in interocular phase. Because disparity modulations are hardly distinguishable above 5 Hz (Regan and Beverley 1973a, 1973b), we chose a rather low stimulation frequency (i.e., 1F = 2.12 Hz) to elicit strong responses in our two conditions and to facilitate the comparison between the underlying cortical mechanisms.

## MATERIALS AND METHODS

*Subjects.* Fourteen subjects (9 men, 5 women, age range 22–69 yr) participated in the main experiment. They were volunteers and had normal stereopsis and normal or corrected-to-normal visual acuity. All subjects were given instructions and detailed information about the experiments. They provided written, informed consent before participating in the study in accordance with Helsinki Declaration; the human subjects review committee of Smith-Kettlewell Eye Research Institute approved the study.

*Stimulus.* This study compared steady-state EEG responses for two conditions: *1*) random dots undergoing lateral motion; and *2*) random dots moving in depth. For both, orthogonally polarized images from two matched Sony Trinitron monitors (model 110GS) were combined via a beam splitter system and viewed binocularly through appropriately oriented polarized filters placed immediately in front of the eyes. Each eye could see the image from only one screen; the viewing distance was 80 cm. The two half-images consisted of black backgrounds filled with the bright random dots (contrast: 90%, and density: 20 dots per square degree of visual field). The total stimulus area was a 16.25° square. Inside this square was another square (13.8° on a side) that was divided into six segments that alternated between moving and stationary, beginning at the bottom with a stationary segment (see Fig. 1). Dots localized within the three moving segments moved laterally (left and right) every 472 ms (1F = 2.12 Hz) following a square-wave input of 4 arcmin of magnitude. The retinal displacement in each eye was exactly the same for the two conditions except for interocular phase. In the lateral motion condition, dots moved in phase between the two eyes, and the three bars were perceived as moving laterally (4 arcmin from left to right and 4 arcmin from right to left). In the MID condition, dots moved out-of-phase between the two eyes and the three bars were perceived as moving in depth between 4 arcmin uncrossed and 4 arcmin crossed. The stimulation frequency was identical to the one used in our previous studies (Cottereau et al. 2012b, 2012c). At this frequency, our stimuli moved at a speed of $0.28°\cdot s^{-1}\cdot eye^{-1}$.

To facilitate fusion of the two monocular images, the stimuli also contained a pair of nonius lines (one in each eye) and a binocularly visible fixation point superimposed on the center of the screen (see Fig. 1). The subject task was to fixate this point during the recordings. The nonius lines, combined with the fixation point and the large static background constituted a stable zero-disparity reference that permitted the subjects to maintain their fixation at the horopter during the motion step of the bars. To assess the stability of fixation, we asked our subjects if they experienced misalignment of the nonius lines during the recordings. All of them reported that the lines remained aligned. Given that the sensitivity for nonius misalignment is typically below 2 arcmin (McKee and Levi 1987), we conclude that eye position was not driven by the stimulus. To test if our results were affected by the chosen disparity values, we recorded responses to the exact same stimuli, except that the bars had a disparity offset of either 6 arcmin or 10 arcmin uncrossed in 10 of our 14 subjects. For the first offset, the bars were therefore either moving laterally at 6 arcmin uncrossed, or were moving in depth from 10 to 2 arcmin uncrossed. For the second offset, the bars were either moving laterally at 10 arcmin uncrossed, or were moving in depth from 14 to 6 arcmin uncrossed. For each experimental condition, the EEG stimulus presentation lasted 10.35 s (which is 22 cycles of the bar motion modulation); the first 940 ms (i.e., the first 2 cycles) of the data record were discarded to avoid start-up transients, leading to 9.41-s trials (i.e., 20 cycles of the disk disparity modulation). Trials for the different conditions were run interspersed in random order in 10-min blocks. The blocks were repeated four times, producing a total of 20 trials per condition.

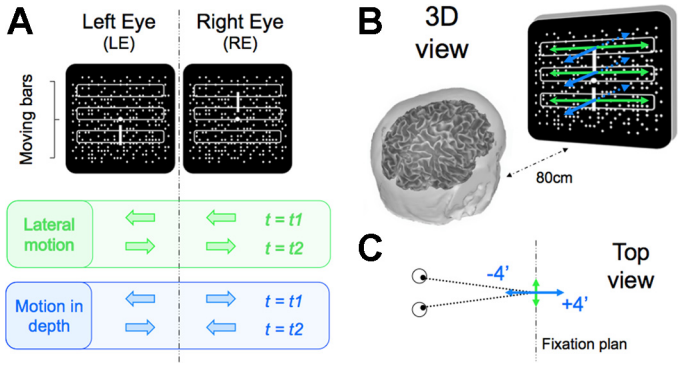


Fig. 1. Diagram of stimulus configuration. The horizontal bars are shown in white here for illustration, but were only detectable from motion cue in the real display. *A*: the two monocular images and a schematic representation of the two conditions. Dots within the three horizontal bars moved laterally (2.12 Hz square motion of 4 arcmin), either in phase between the two eyes (lateral motion condition), or out of phase between the two eyes (motion in depth condition). *B*: three-dimensional (3D) view. *C*: top view and detail of the dot displacement.

*EEG signal acquisition and preprocessing.* The EEG data were collected with 128-sensor HydroCell Sensor Nets (Electrical Geodesics, Eugene, OR) and were band-pass filtered from 0.1 to 200 Hz. Following each experimental session, the 3D locations of all electrodes and three major fiducials (nasion, left and right periauricular points) were digitized using a 3Space Fastrack 3D digitizer (Polhemus, Colchester, VT). For all observers, the 3D digitized locations were used to coregister the electrodes to their T1-weighted anatomical magnetic resonance imaging (MRI) scans and to construct the EEG forward model (see *Forward modeling of the current source* section). Raw data were evaluated off line according to a sample-by-sample thresholding procedure to remove noisy sensors that were replaced by the average of the six nearest spatial neighbors. On average, less than 5% of the electrodes were substituted; these electrodes were mainly located near the forehead or the ears. The substitutions had a negligible impact on our results, as recordings at occipital and parietal locations primarily drive our estimates of the responses within the visual ROIs. After this operation, the EEG was re-referenced to the common average of all the sensors. Within each 9.41-s trial, the data were segmented into five 1.82-s long epochs (i.e., each of these epochs was exactly 4 cycles of the bar motion modulation). EEG epochs that contained a large percentage of data samples exceeding a noise threshold (depending on the subject and ranging between 25 and 50 $\mu$V) were excluded from the analysis on a sensor-by-sensor basis. This was typically the case for epochs containing artifacts, such as blinks or eye movements. The use of steady-state stimulation drives cortical responses at specific frequencies directly tied to the stimulus frequency. It is thus appropriate to quantify these responses in terms of both phase and amplitude. Therefore, a Fourier analysis was applied on every remaining epoch using a discrete Fourier transform with a rectangular window. Given the time length of an epoch (i.e., 1.82 s), this Fourier transformation led to a frequency resolution of $\delta f = 0.55$ Hz. For each frequency bin, the Fourier coefficients were then averaged across all the epochs and all the trials. Thus these average Fourier coefficients were obtained from up to 100 (5 epochs $\times$ 20 trials) values.

*Structural and fMRI.* Structural and fMRI scanning was conducted at 3T (Siemens Tim Trio, Erlangen, Germany) using a 12-channel head coil. We acquired a T1-weighted MRI dataset (3D MP-RAGE sequence, $0.8 \times 0.8 \times 0.8$ mm$^3$) and a 3D T2-weighted dataset (SE sequence at $1 \times 1 \times 1$ mm$^3$ resolution) for tissue segmentation and registration with the functional scans. For fMRI, we employed a

single-shot, gradient-echo planar imaging sequence (repetition time/echo time = 2,000/28 ms, flip angle 80°, 126 volumes per run) with a voxel size of $1.7 \times 1.7 \times 2$ mm$^3$ ($128 \times 128$ acquisition matrix, 220 mm field of view, bandwidth 1,860 Hz/pixel, echo spacing 0.71 ms). We acquired 30 slices without gaps, positioned in the transverse-to-coronal plane approximately parallel to the corpus callosum and covering the whole cerebrum. Once per session, a 2D SE T1-weighted volume was acquired with the same slice specifications as the functional series to facilitate registration of the fMRI data to the anatomical scan. The general procedures for these scans (head stabilization, visual display system, etc.) are standard and have been described in detail elsewhere (Brewer et al. 2005). The FreeSurfer software package (http://surfer.nmr.mgh.harvard.edu) was used to extract both gray/white and gray/cerebrospinal fluid (CSF) boundaries. These surfaces can have different curvatures. In particular, the gray/white boundary has sharp gyri (the curvature changes rapidly) and smooth sulci (slowly changing surface curvature), while the gray/CSF boundary is the inverse, with smooth gyri and sharp sulci. To avoid these discontinuities, we generated a surface partway between these two boundaries that has gyri and sulci with approximately equal curvature. This "midgray" cortical surface consisted of a very dense triangular tessellation of several hundred thousand regularly spaced vertices. This tessellation was then down-sampled to 20,484 vertices using the MNE software package (http://www.nmr.mgh.harvard.edu/martinos/userInfo/data/sofMNE.php). This number is low enough to compute the forward model on a standard workstation and yet accurately reflect the shape of cortical manifold (see e.g., Baillet et al. 2001). The final "midgray" surface was used to define the visual ROIs and the source space for the EEG current modeling (see the *Forward modeling of the current source* and *Inverse modeling constrained by the visual ROIs* sections).

*Functional and anatomical area definition.* Retinotopic field mapping using rotating wedges and expanding/contracting rings produced ROIs defined by the visual cortical areas V1, V2v, V2d, V3v, V3d, V3A, and V4 in each hemisphere (Wade et al. 2002). ROIs corresponding to hMT+ were identified using low-contrast motion stimuli similar to those described by Huk and Heeger (2002). The LOC was defined using a block-design fMRI localizer scan. During this scan, the observers viewed blocks of images depicting common objects (12 s/block), alternating with blocks containing scrambled versions of the same objects. The stimuli were those used in a previous study (Kourtzi and Kanwisher 2000). The regions activated by these scans included an area lying between the V1/V2/V3 foveal confluence and hMT+ that we identified as LOC. This definition covers almost all regions (e.g., V4d, LOC, LOp) that have previously been identified as lying within object-responsive lateral occipital cortex (Kourtzi and Kanwisher 2000).

Using the FreeSurfer software package (see the *Structural and fMRI* section), we automatically subdivided the cortex mesh of each subject into 64 anatomically based regions (Desikan et al. 2006). The superior and inferior parietal parcellations were used to characterize the cortical activity outside our functionally defined visual ROIs.

*Forward modeling of the current source.* For each subject, the EEG source space was given by his "midgray" cortical surface tessellation (see the *Structural and fMRI* section) and consisted in 20,484 regularly spaced vertices. The distance between connected vertices was on average 3.7 mm, with a standard deviation of 1.5 mm, range 0.1–11 mm. Current dipoles were placed at each of these vertices. Their orientations were constrained to be orthogonal to the cortical surface to diminish the number of parameters to be estimated in the inverse procedure (Hämäläinen et al. 1993). The FSL toolbox (http://www.fmrib.ox.ac.uk/fsl/) was used to segment, from the individual T1 and T2 weighted MRI scans, contiguous volume regions for the inner skull, outer skull, and scalp. These MRI volumes were then converted into inner skull, outer skull, and scalp surfaces (Smith 2002; Smith et al. 2004) that defined the boundaries between the brain/CSF and the skull, the skull and the scalp, and the scalp and the air. The source space, the 3D electrode locations, and the individually defined boundaries were then combined using the MNE software package to characterize the electric field propagation using a three-compartment boundary element method (Hämäläinen and Sarvas 1989). The resulting forward model is linear and links the activity of the 20,484 cortical sources to the voltages recorded by our EEG electrodes.

*Inverse modeling constrained by the visual ROIs.* Cortical current density estimates of the neural responses were obtained from an L2 minimum-norm inverse of the forward model described above (Hämäläinen et al. 1993). We used the definition of the visual ROIs to constrain these estimates by modifying the source-covariance matrix. Our aim was to decrease the tendency of the minimum-norm procedure to smooth activity over very large surfaces and across different functional ROIs. Two modifications were applied: *1*) we increased the variance allowed within the visual ROIs by a factor of two relative to other vertices; and *2*) we enforced a local correlation constraint within each ROI using the first- and second-order neighborhoods on the cortical tesselation with a weighting function equal to 0.5 for the first order and 0.25 for the second. This correlation constraint, therefore, respects both retinotopy and areal boundaries and permitted us to dissociate the signals from different ROIs, unlike other smoothing methods, such as LORETA, that apply the same smoothing rule throughout cortex (Pascual-Marqui et al. 1994). The details of this approach can be found in Cottereau et al. (2012a). For each subject and condition, this inversion scheme was applied to the average Fourier coefficients (see the *EEG signal acquisition and preprocessing* section) and led to an estimation of these coefficients for each source of the cortical tessellation. Within each functionally defined ROI, the coefficients were then averaged across all the sources belonging to the ROI.

*Cross talk.* In our previous papers (Cottereau et al. 2011, 2012a, 2012b), we have characterized the theoretical cross talk among visual ROIs obtained with our inverse approach. Cross talk refers to the neural activity generated in other ROIs that is attributed to a particular ROI, due to the smoothing of the electric field by the head volume. While our technique provides reliable estimates of the activity within ROIs V1, V4, LOC, hMT+, and V3A, we showed that ROIs V2 and V3 suffered from significant cross talk. These ROIs were therefore excluded from our analysis.

*Cross-subject surface averaging and characterization of the activity within anatomically defined ROIs of the parietal cortex.* Cross-subject, surface-based averaging was used to check if significant activity was evoked by our stimuli outside our functionally defined ROIs. Averaging was performed with the Freesurfer image analysis suite (http://surfer.nmr.mgh.harvard.edu/) as documented in Fischl et al. (1999) and Yeo et al. (2010a, 2010b). First, each subject's cortical surface was inflated to a sphere. Using the pattern of gyral and sulcal curvature, each subject's cortical surface was then aligned to a reference subject. This alignment defines a unique unidirectional transform from every single subject to the target subject. The alignment was then used to average the source data across subjects. For cross-subject, surface-based averaging only, the source reconstructions were smoothed over first- and second-order neighboring vertices; this resulted in a boxcar smoothing with a 4-mm width. Because activity was found outside our functionally defined ROIs in the parietal cortex (see the RESULTS section), we used two anatomically defined ROIs (see the *Functional and anatomical area definition* section) to characterize it: the inferior and the superior parietal cortex. These ROIs did not overlap any of the occipital ROIs. As for functionally defined ROIs, responses in these anatomical ROIs were obtained by averaging the coefficients across all of the sources belonging to the ROI.

*Signal-to-noise ratio analysis.* We were particularly interested in the ROI response magnitudes (i.e., the modules of the Fourier coefficients) at the odd (first and third) and even (second and fourth) components of the steady-state frequency (1F = 2.12 Hz and 3F = 6.36 Hz for odd components and 2F = 4.24 Hz and 4F = 8.48 Hz for

even components). This choice was motivated by the fact that significant responses were still observable in our spectra for the third and fourth harmonics (but not for the fifth and sixth, see the *Responses at the sensor and cortical level* section in RESULTS). Both the first and third components reflect the asymmetries in the neural responses to our stimuli. To obtain a single value that would quantify these asymmetries, the modules of the Fourier coefficients at the first and third harmonics were pooled together using their root-mean-square value. This operation is equivalent to summing the powers of the individual harmonics and then taking the square root (Appelbaum et al. 2006). To take into account the difference of noise levels between the recordings from each of our subjects (Vialatte et al. 2010), we then computed the signal-to-noise ratio (SNR) at odd harmonics by dividing this pooled value by the root mean square of the associated noise magnitudes (Cottereau et al. 2011). Noise magnitude for the first harmonic was given by the average of the moduli at the two neighboring frequencies (i.e., $1F - \delta f$ and $1F + \delta f$, where $\delta f = 0.55$ Hz is the frequency resolution of our Fourier analysis). Similarly, noise magnitude at the third harmonic was given by the average of the moduli at $(3F - \delta f)$ and $(3F + \delta f)$. For a given subject and a given frequency, the noise magnitude was averaged across all the conditions belonging to the same recording session. The SNRs at even harmonics (that reflect the symmetries in the neural responses to our stimuli) were obtained by repeating the same computation for the second (2F) and fourth (4F) components of the steady-state frequency. In the following, SNRs at odd and even harmonics are presented in decibels ($20 \times \log_{10}$). We tested the statistical significance of the SNRs obtained for lateral motion and MID at the odd and even harmonics, using repeated measure analyses of variance (ANOVA). We specifically tested for main effects of the two stimulus conditions, the ROIs and for their interaction. Given a significant interaction, we made post hoc comparisons using pairwise *t*-tests. The equal variance assumption underlying the validity of the ANOVAs was evaluated with Mauchly's sphericity test. The sphericity tests were not significant, so we did not correct the *P* values for the ANOVAs.

*Phase analysis.* From the Fourier coefficients, we also obtained the temporal phases associated with different ROIs. Newly developed techniques (Berens et al. 2008; Tolias et al. 2007) were used to calculate confidence intervals for the average value of our phase distributions across subjects (Zar 1999, their Eqs. 26.23–26.26). We performed these computations using the circular statistics toolbox (Berens 2009). Only the phases at the first and second harmonics were computed, as it was not possible to obtain reliable phase values for circular statistics at frequencies corresponding to the third and fourth harmonics (i.e., 6 and 8 Hz, respectively). To test whether the phase distributions corresponding to the different conditions were uniform, we performed Rayleigh tests (Fisher 1995). To test whether phase differences existed between the ROIs, we performed a Watson-Williams test, which is a circular analog of the one-factor ANOVA (Stephens 1969; Watson and Williams 1956). It tests the null hypothesis that all of the groups (i.e., in our case, the phase within the five visual ROIs) share a common direction. Finally, to test the influence of two factors simultaneously (in our case, ROI and condition), we used a Harrison-Kanji test (Harrison and Kanji 1988), which is a circular analog of two-factor ANOVA.

*Connectivity analysis.* We were also interested in the functional connectivity between ROIs. Connectivity values are usually computed for each individual subject from a single-trial analysis. Because it is difficult to obtain a reliable estimate of the responses within a given ROI at the single-trial level, we characterized the connectivity at the group level. For each pair of ROIs *i* and *j*, the connectivity at a given frequency was computed by *1*) calculating for each individual subject the difference between the Fourier coefficients associated with ROI *i* and ROI *j*; and *2*) computing the weighted phase-locking index (wPLI; see Vinck et al. 2011) of these differences across subjects. The wPLI is similar to the classical phase-locking value (see Lachaux et al. 1999), but avoids false alarms caused by volume conduction. It is therefore a useful metric to compute synchrony at the cortical level. To be certain that our estimated wPLI reflected a real connectivity (i.e., a consistent phase covariation between two ROIs across subjects) rather than an evoked mechanism (e.g., two ROIs whose phases are directly driven by the stimulus but that are not directly related), we performed permutation tests. For each pair of ROIs *i* and *j*, the permuted wPLI distribution was computed by shuffling the subjects (e.g., the Fourier coefficients were taken from *subject 1* for ROI *i* and from *subject 2* for ROI *j*). Only the pairs of ROIs whose wPLI was above the 95 percentile of the permuted wPLI distribution were considered as reflecting real connectivity. wPLI values were computed between all of the combinations of our five visual ROIs for the first and second harmonics to complete the phase analysis described above.

## RESULTS

*Responses at the sensor and cortical level.* Our stimulation rate of $1F = 2.12$ Hz is low enough to produce evoked responses that have highly structured temporal waveforms, as well as characteristic, steady-state response spectra. Figure 2*A* shows the "butterfly" plots of the activity evoked by lateral motion and MID during one cycle of the steady-state stimulation. This plot shows all channels (average reference) superimposed on a common time base.

Although the two stimuli differed only in interocular phase, they evoked very different responses. The butterfly plot of the response to lateral motion is very symmetric, meaning that the global response to leftward motion is equivalent to the global response to rightward motion. The butterfly plot of the responses to MID has less amplitude and is asymmetric, possibly reflecting differences between the cortical responses to forward and backward motion. In a steady-state experiment, it is, however, more convenient to study the responses in the frequency domain where the knowledge of the driving frequency of the stimulus permits to extract meaningful characteristics of the responses (in terms of both amplitude and phase) on the basis of these symmetry considerations. Figure 2*B* shows the amplitude spectra for a representative occipital electrode. For lateral motion, we can see that only the second and fourth harmonics have amplitudes above the noise level. For MID, these even harmonics are also of large amplitude, but we can also observe signals at the first and third harmonics. Figure 2, *C* and *D*, characterizes the topographic maps and associated cross-subject surface average reconstruction corresponding to these four odd and even harmonics. Although our stimuli mostly evoke activity within the occipital cortex where our functionally defined ROIs are localized (see Fig. 3*A*), some activity can also be observed in the parietal cortex (e.g., for the responses to MID at 1F for the responses to lateral motion at 2F). In the following, we first analyze the responses within our functionally defined ROIs (see the following sections), and then we analyze the responses of two anatomically defined ROIs: the inferior and superior parietal cortex. Because the second and fourth harmonics both characterize symmetries in the response and because the associated topographic maps and source reconstructions show similar patterns, we pooled these harmonics together using the SNR (see the *Signal-to-noise ratio analysis* section). The same operation was done for the first and third harmonics.

*Time courses and SNRs in the visual ROIs.* Figure 3*B* shows the time courses of the responses in the visual ROIs.

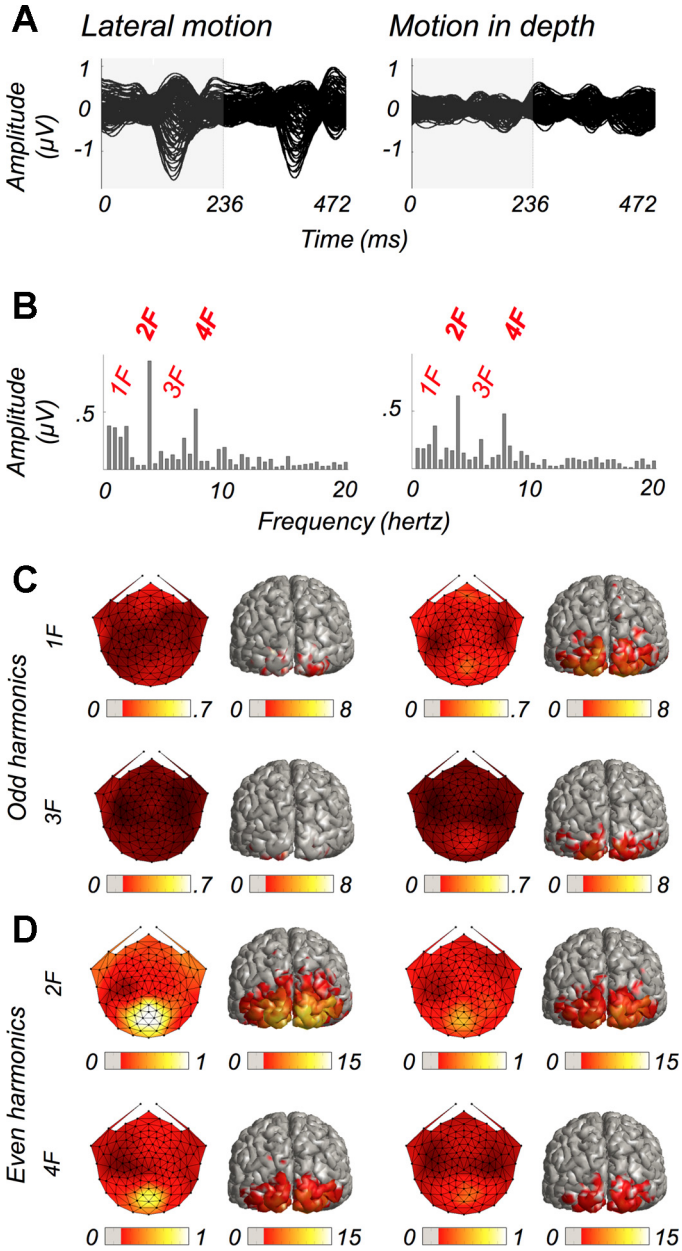


Fig. 2. Activity evoked by lateral motion (*left*) and motion in depth (*right*) at the sensor and cortical levels. *A*: butterfly plots of the activity on the 128 electrodes during one cycle (i.e., 472 ms) of the steady-state stimulation. Curves have been filtered to remove frequencies above 20 Hz. The time windows corresponding to the two perceptual states are indicated using different color codes: gray when the bars are moving leftward (for lateral motion) or backward (for motion in depth; at time $t = 0$), and white when they are moving rightward (for lateral motion) or forward (for motion in depth; at $t = 236$ ms). *B*: amplitude spectrum of one typical occipital electrode. Amplitudes for frequency bins up to 20 Hz are presented (spectral resolution of 0.55 Hz). The four first harmonics of the stimulation frequency have been marked in red to emphasize the precise time-locking of the steady-state visual evoked potential. Topographic maps (units of $\mu$V) and associated surface-based average cortical activity (units of $\mu$A/mm$^2$) for the odd (*C*; i.e., first and third) and even (*D*; i.e., second and fourth) harmonics of the stimulation frequency are shown. The cortical surfaces are presented from behind to focus on the activated regions, which are in the occipital and parietal cortex. For cortical activity, only the sources whose activity is above 20% of the most responsive source (across the two frequencies and two conditions) are shown.

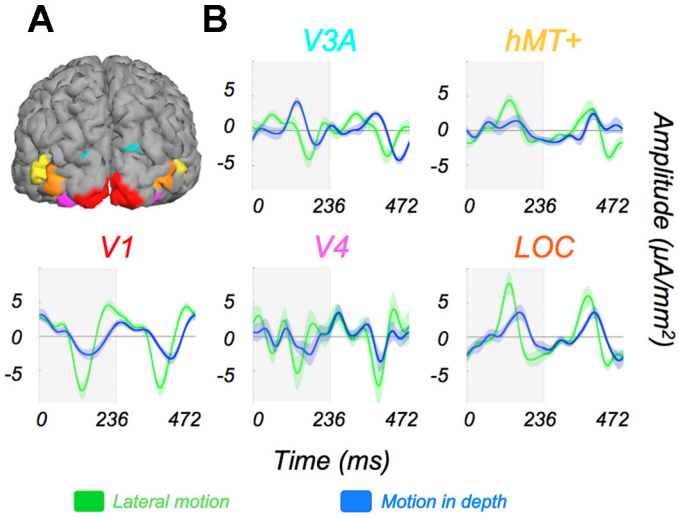


Fig. 3. Time courses in our five visual regions of interest (ROIs). *A*: localization of V1, V4, lateral occipital complex (LOC), V3A and hMT+ in one typical subject. *B*: average waveforms corresponding to lateral motion and motion in depth in our ROIs ($n = 14$ subjects). Curves have been filtered to remove frequencies above 20 Hz. The shaded areas around the curves correspond to the standard errors. The time windows corresponding to the two perceptual states are indicated using different color codes: gray when the bars are moving leftward (for lateral motion) or backward (for motion in depth; at $t = 0$), and white when they are moving rightward (for lateral motion) or forward (for motion in depth; at $t = 236$ ms).

Figure 4 shows the SNR values at both the odd and even harmonics for the two conditions.

We first consider the SNRs for odd harmonics (Fig. 4*A*). If the odd harmonic SNRs for lateral motion were negligible (a SNR of 6 dB corresponds to a linear factor of 2), higher values were obtained for MID. This difference between the SNRs obtained for MID and lateral motion was confirmed by an ANOVA (2 conditions $\times$ 5 ROIs) that showed a significant effect of the condition ($P = 0.009$). The effect of the ROIs and the interaction between conditions and ROIs were not significant. The odd harmonics observed here for MID are consistent with the population-level disparity tunings we measured in a previous study (Cottereau et al. 2011). In that study, responses in the crossed domain were larger than those in the uncrossed domain. This result suggests that the SNRs obtained for MID at the odd harmonics are at least partially driven by disparity-responsive neural populations (see also DISCUSSION).

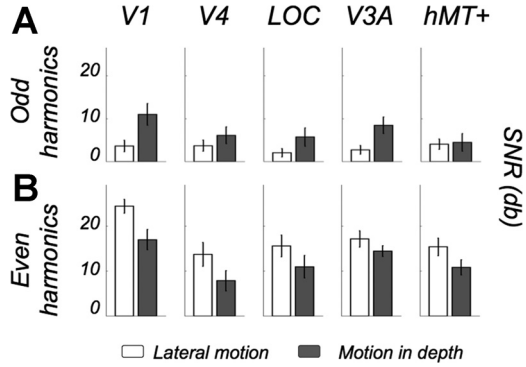


Fig. 4. Signal-to-noise ratios (SNRs) of the responses. *A*: SNRs of the odd (i.e., first and third) harmonic responses averaged over 14 subjects; lateral motion (white bars) and motion in depth (gray bars) are shown. The error bars provide the standard errors. *B*: SNRs at even (i.e., second and fourth) harmonics.

The even harmonics reflect the part of the total response that is equivalent for leftward and rightward motion (in the lateral motion condition) and for backward and forward motion (in the MID condition). Figure 4*B* shows the SNR values at the even harmonics for the two conditions. For both lateral motion and MID, the SNR values are much larger at the even harmonics (note the scale difference between Fig. 4, *A* and *B*), consistent with the symmetric shape of the time courses (see Fig. 3). To test if significant differences existed between these values, we performed an (2 conditions × 5 ROIs) ANOVA that showed significant effects of condition ($P$ = 4.34e-5) and ROI ($P$ = 4.69e-6). The interaction between conditions and ROIs was not significant. The condition effect is driven by the stronger SNRs obtained in every ROI for lateral motion compared with MID. SNRs for lateral motion are about 6 dB (i.e., 2 times in linear scale) above those obtained for MID.

*Phase analysis.* To test for possible differences in the timing of responses to lateral motion and MID, we analyzed the phase of the first and second harmonics derived from the respective complex-valued Fourier coefficients. Phases at the first harmonic were not consistent enough across subjects to define a 95% confidence interval for the average (see the *Phase analysis* section). These data are therefore not shown. Figure 5 displays the phases at the second harmonic as a Nyquist plot.

In all cases, it was possible to define a 95% confidence interval for the average phase difference between lateral motion and MID. In the V1 ROI, the average difference is 27.66° with a confidence interval of [1.9°, 53.4°]. This phase difference is consistent with either a lag for MID relative to lateral motion of 18 ms or a lead of 218 ms. Given the time intervals, it seems more plausible that it represents a lag rather than a lead. Beyond the V1 ROI, the average phase difference is 52.5°, 32.2°, 77.8° and 43.3° in ROIs V4, LOC, V3A and hMT+, respectively (with confidence intervals of [−2.1°, 107°], [3°, 61.3°], [49°, 106.7°] and [−7.9°, 94.4°]). The corresponding lags in time are 34 ms in the V4 ROI, 21 ms in the LOC ROI, 51 ms in the V3A ROI and 28 ms in the hMT+ ROI.

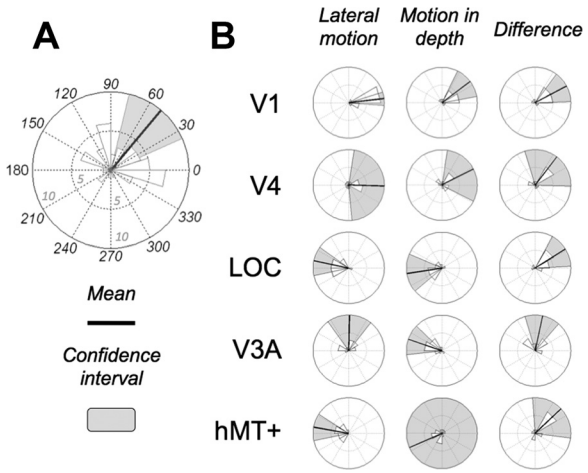


Fig. 5. Histograms of the phases at the second harmonic (i.e., 2F = 4.24 Hz; $n$ = 14 subjects). *A*: example of histogram. Phases are presented in degrees on the trigonometric circle (anticlockwise progression). The number of data points (one data point is the phase value for one subject) included in each portion of the histograms is provided by the radius of the wedges. The inner and outer circles correspond to 5 and 10 data points, respectively. In this example, 5 subjects have their phases comprised between 0 and 18°. The thick lines give the mean of the distribution, and the shadowed portions outline the 95% confidence interval for this mean. The histograms lacking shaded wedges refer to phases whose confidence intervals cannot be reliably estimated. *B*: phases of the different ROIs for lateral motion and motion in depth. The phase difference (i.e., lateral motion − motion in depth) is displayed in the last column.

The phase histograms suggest that, even when averaged across subjects, the distributions of these phase difference are centered on specific values in different ROIs. These results were confirmed by Rayleigh tests where the $P$ values for the V1, LOC, V3A and hMT+ ROIs were equal to 1.2e-4, 6.6e-4, 5.8e-4 and 0.04 respectively, meaning that the phase differences in these ROIs were significantly different from a uniform distribution. The test was nearly significant in the V4 ROI with a $P$ value of 0.058. The Watson-Williams test also demonstrated that there was a statistically significant main effect of the ROI (the null hypothesis is rejected with $P$ = 0.0199). This main effect is principally driven by the larger phase lags in the V3A ROI and to a lesser degree in the V4 and hMT+ ROIs. Our phase analysis therefore suggests that, although our stimuli only differed in their interocular phase, the dynamics of the responses they evoked are very different, with the responses to MID being significantly lagged compared with responses to lateral motion. This lag starts as early as the V1 ROI (27.66°) and increases in higher visual ROIs like V3A and possibly V4 and hMT+.

*Connectivity analysis.* Using the wPLI (see the *Connectivity analysis* section), we characterized the connectivity between our five visual ROIs for both lateral motion and MID at the first and second harmonics. For each of these conditions, 10 different pairings were possible: V1/V4, V1/LOC, V1/V3A, V1/hMT+, V4/LOC, V4/V3A, V4/hMT+, LOC/V3A, LOC/hMT+ and V3A/hMT+. From our permutation tests, we did not find significant connectivity at the first harmonic. At the second harmonic, we established that the V1/LOC ROI pair was significantly connected for both lateral motion and MID. This result means that, for these two conditions, phase values in the V1 ROI covary with phase values in the LOC ROI across subjects. We also found significant connectivity between the V3A ROI and the hMT+ ROI for MID at the second harmonic.

*Effects of the disparity offset from the fixation plane.* Our results clearly establish that responses to lateral motion and MID are different in all our ROIs. To determine whether these differences are specific to motion within and across the fixation plane or to the chosen disparity values, we repeated the measurements with different disparity pedestals.

We recorded the responses to the exact same stimuli in 10 of our 14 subjects, except that the bars had a pedestal disparity of either 6 arcmin or 10 arcmin uncrossed. As in our first two conditions, lateral motion and MID had identical monocular half-images and only differed by the interocular retinal displacement. For the first offset value, we therefore compared the responses evoked by the bars moving laterally at 6 arcmin to the responses elicited by the bars moving in depth between 10 and 2 arcmin uncrossed. For the second offset value, we compared the responses evoked by the bars moving laterally at 10 arcmin to the responses elicited by the bars moving in depth between 6 and 14 arcmin uncrossed. Before describing the effect of the disparity pedestals on the differences between lateral motion and MID, we will characterize the effect of these pedestals on the lateral motion and MID responses separately. Figure 6*A* shows responses at odd and even harmonics corresponding to a lateral motion at three different disparity offsets.

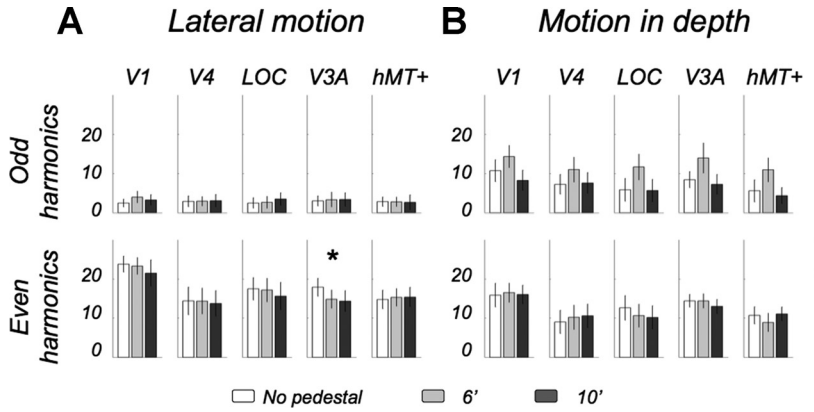


Fig. 6. SNRs for lateral motion and motion in depth from three different disparity offsets (0, 6 and 10 arcmin; $n = 10$ subjects). *A*: SNRs at the odd (*top*) and even (*bottom*) harmonics in our five ROIs for lateral motion. The error bars provide the standard errors. *Significant differences in the V3A ROI responses at even harmonics (see details in the text). *B*: SNRs for motion in depth.

To test if the disparity pedestals had an effect on the odd harmonics responses to lateral motion, we performed an (3 pedestal conditions × 5 ROIs) ANOVA that did not lead to any significant effect of condition, ROI or interaction. To test if the disparity pedestals had an effect on the even harmonics responses to lateral motion, we performed an (3 pedestal conditions × 5 ROIs) ANOVA that showed a significant effect of ROI ($P = 0.001$) and a significant interaction ($P = 0.022$). This interaction was driven by the responses in the V3A ROI as post hoc pairwise *t*-tests showed that this ROI had stronger SNRs for a 0 arcmin pedestal ($P = 0.01$ for the comparison between responses from 0 and 6 arcmin pedestals and $P = 0.03$ for the comparison between responses from 0 and 10 arcmin pedestals). This effect can be seen in the times courses estimated in the V3A ROI that are shown in Fig. 7*A* (responses in the V1 ROI are also shown for comparison). Harrison-Kanji tests (see the *Phase analysis* section) did not find any effect of the pedestals on phase values at both odd and even harmonics. Significant connectivity between ROIs V1 and LOC were found for every disparity pedestal.

Figure 6*B* shows responses at odd and even harmonics corresponding to MID at three different pedestals. At the odd harmonics, an ANOVA (3 pedestal conditions × 5 ROIs) showed a significant effect of the condition ($P = 0.01$). This effect is explained by the fact that, with a 6 arcmin offset, odd responses to MID were stronger in all the ROIs. This result is consistent with the disparity tuning functions we measured previously (Cottereau et al. 2011), where asymmetries in every ROI were larger between 2 and 10 arcmin uncrossed than either between 4 arcmin crossed and 4 arcmin uncrossed or between 6 and 14 arcmin uncrossed (see Fig. 7*B* for an illustration in ROIs V1 and V3A). For the even harmonics, an ANOVA (3 offset conditions × 5 ROIs) showed a significant effect of ROI ($P = 0.02$), but the pedestals did not significantly affect the phase values at odd or even harmonics (i.e., no effect were found using Harrison-Kanji tests). Significant connectivity between ROIs V1 and LOC and between ROIs V3A and hMT+ was found for every disparity pedestal.

Overall, the disparity pedestals mainly affected the SNR values at the odd harmonics (an effect was also found in the V3A ROI at even harmonics for lateral motion) and did not change the estimated phases and connectivity. Importantly, the changes in the SNRs did not affect the conclusion we made on the difference between responses to lateral motion and MID from our analysis of the data obtained from the 14 subjects with a 0 arcmin offset (see the *Signal-to-noise ratio analysis* section). Indeed, a direct comparison between responses to lateral motion and MID at the two different disparity offsets led to significant effect of the condition at odd (bigger SNR for MID, $P = 0.008$ for a 6 arcmin offset and $P = 0.04$ for a 10 arcmin offset) and even (bigger SNRs for lateral motion, $P = 0.003$ for a 6 arcmin offset and $P = 0.034$ for a 10 arcmin offset) harmonics (see Fig. 4).

The phase differences observed at the second harmonics are provided in Table 1.

Consistent with the fact that the disparity pedestals did not affect the phase of the responses to lateral motion and MID separately, they did not change the phase difference between these two conditions. For both a 6 and a 10 arcmin offset, responses in all the ROIs (including the V1 ROI) were lagged for MID. These results were supported by Rayleigh tests that

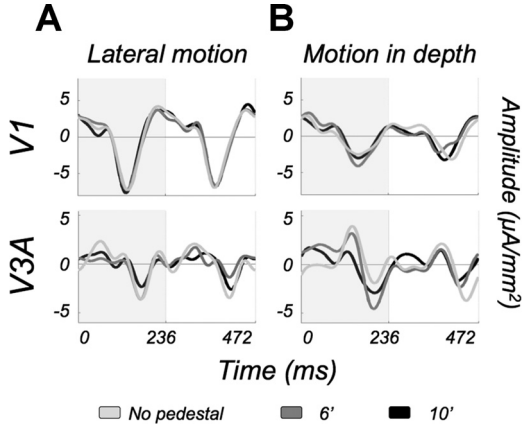


Fig. 7. Time courses of the responses from different disparity offsets in two representative ROIs: V1 and V3A. *A*: responses to lateral motion. *B*: responses to motion in depth. See Fig. 3 for the details of the legend.

Table 1. *Phase difference between lateral motion and motion in depth from different disparity offsets at the second harmonics*

| ROIs/Offsets | No Offset, ° | 6 arcmin Offset, ° | 10 arcmin Offset, ° |
|---|---|---|---|
| V1 | 32 [−5, 70] | 25 [2, 49] | 30 [2, 58] |
| V4 | 51 [17, 68] | 50 [14, 87] | 58 [16, 101] |
| LOC | 31 [1, 62] | 41 [28, 55] | 27 [10, 45] |
| V3A | 75 [42, 108] | 59 [25, 92] | 57 [11, 105] |
| hMT+ | 42 [11, 74] | 41 [9, 74] | 62 [19, 106] |

$n = 10$ subjects. Nos. give the average phase difference in degrees, while the two nos. in the brackets provide the 95% confidence interval. ROIs, regions of interest; LOC, lateral occipital complex.

confirmed that the phase values in every ROI were nonuniformly distributed. For the two disparity pedestals, Watson-Williams tests also generally confirmed that lags were different in the different ROIs ($P = 0.06$ and $P = 0.03$ for the 6 and 10 arcmin pedestals, respectively). The lags in higher visual ROIs like V3A, hMT+ or V4 are larger than those in the V1 ROI. As a reminder, the ~30° phase difference observed in the V1 ROI for the 3 offsets corresponds to either a lag for MID of 20 ms or a lead of 216 ms, while the ~65° phase difference observed in the V3A ROI corresponds to either a lag for MID of 43 ms or a lead of 193 ms. As we noted above, it seems more likely that these phase differences represent a lag rather than a lead.

*Cortical responses outside the functional ROIs.* We saw in Fig. 2 that, although the cortical activity evoked by our stimuli is mainly localized within our functionally defined ROIs, additional activity exists in the parietal cortex. To characterize these responses, we used a segmentation based on the anatomy (see the *Functional and anatomical area definition* section) to define in each subject two new regions: the inferior and the superior parietal cortex. Figure 8*A* shows these regions in one typical subject.

The inferior and superior parietal ROIs extend on either side of the intraparietal sulcus. Because these ROIs are very broad and also because they are not defined using functional localizers, our source estimation technique is probably less accurate

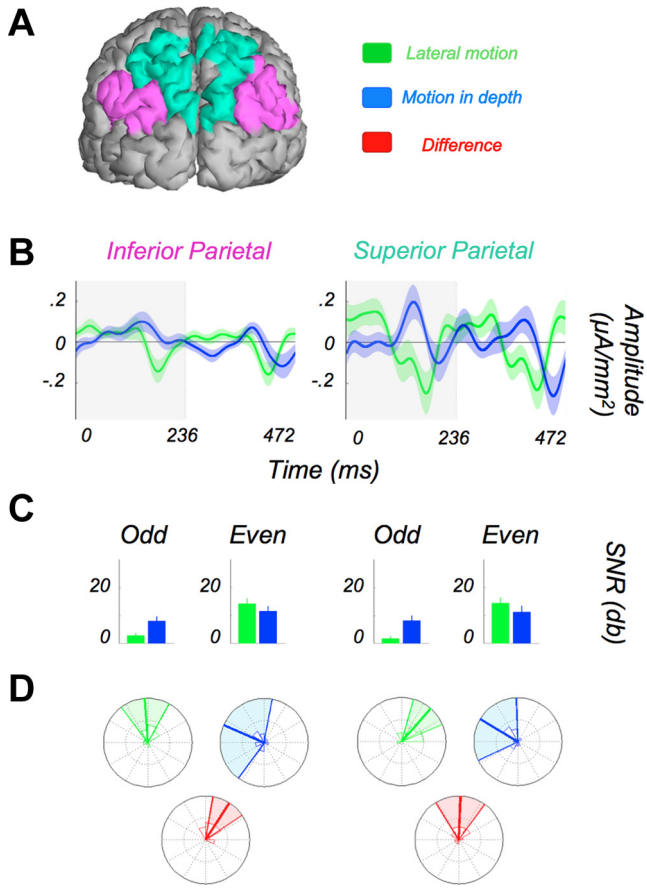


Fig. 8. Responses to lateral motion and motion in depth outside our functionally defined ROIs. *A*: localization of the two studied anatomically defined regions: the inferior parietal cortex and the superior parietal cortex. *B*: time courses estimated in these two regions (see Fig. 3 for the details of the legend). *C*: SNRs for odd and even harmonics. *D*: histograms of the phases at the second harmonic (see Fig. 5 for the details of the legend).

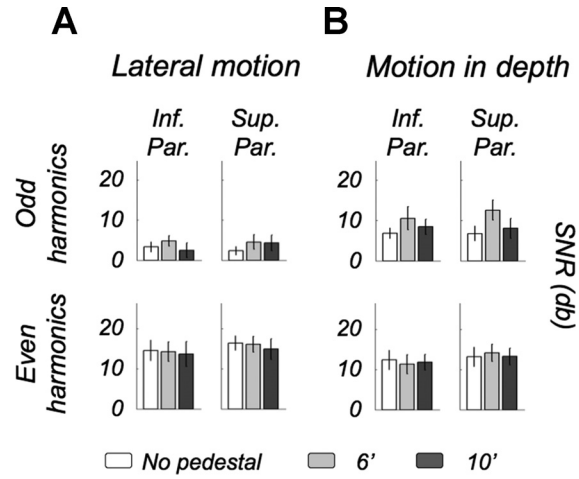


Fig. 9. SNRs for lateral motion (*A*) and motion in depth (*B*) from three different disparity offsets (0, 6 and 10 arcmin) in the inferior (Inf. Par.) and superior (Sup. Par.) parietal cortex ($n = 10$ subjects).

in this case, suggesting that caution is in order regarding the exact origin of the activation described below. However, responses from these two ROIs probably reflect the neural processes from several areas that have previously been described as very responsive to depth. In particular, our superior parietal ROI encompasses the ventral portion of the intraparietal sulcus and the dorsal and medial part of the intraparietal sulcus. It was shown recently that these areas have specific responses to disparity-defined objects (see Durand et al. 2009).

From the estimated time courses (Fig. 8*B*), we see that, while lateral motion leads to very symmetric responses in these two ROIs, responses to MID have a strong asymmetric component, particularly in the superior parietal ROI. The larger SNRs for MID at odd harmonics and for lateral motion at even harmonics were confirmed by ANOVAs (2 conditions × 2 ROIs). Significant condition effects were found for odd ($P = 0.004$) and even harmonics ($P = 0.025$). Our analysis of the phase at the second harmonic (Fig. 8*B*) shows consistent lags (i.e., with $P$ values $< 0.05$ in the Rayleigh test) for the responses to MID in both the two regions. These lags were equal to 57° in the inferior parietal ROI and to 87.8° in the superior parietal ROI with confidence intervals of [34°, 80.2°] and [53.8°, 121.8°], respectively. These phase values are consistent with lags in time of 37 ms in the inferior parietal ROI and of 58 ms in the superior parietal ROI. Interestingly, the lag observed in the superior parietal cortex is even larger than the one measured in our V3A ROI, suggesting that differences in time between the responses to MID and lateral motion increase along the dorsal pathway.

The effects of the disparity offsets on the SNRs estimated in these two ROIs are shown in Fig. 9.

As was seen in the functionally defined ROIs, the offsets only affected the SNRs at odd harmonics for MID. This was confirmed by an (3 offset conditions × 2 ROIs) ANOVA that led to a significant effect ($P = 0.006$) of the condition. The offsets did not affect the phase values. In the inferior parietal ROI, the average phase values (95% confidence intervals) were equal to 53.7° [22.5°, 84.8°], 59.3° [30.7°, 87°] and 57° [11.4°, 102.6°], for offsets of 0, 6 and 10 arcmin, respectively. In the superior parietal ROI, these values were equal to 95.8° [51.8°, 139.9°], 73.2° [45.5°, 101°] and 76.1° [31.4°, 120.8°]. All of

these lags were estimated as reliable according to Rayleigh tests ($P < 0.05$). Consistent with the responses without offset, a direct comparison between responses to lateral motion and MID at the two different disparity offsets led to significant effect of the condition at odd (bigger SNR for MID, $P = 0.003$ for a 6 arcmin offset and $P = 0.01$ for a 10 arcmin offset) and even (bigger SNRs for lateral motion, $P = 0.006$ for a 6 arcmin offset and $P = 0.02$ for a 10 arcmin offset) harmonics. Our connectivity analysis did not detect significant connectivity between the parietal ROIs and any of the other ROI at any of the offset values.

## DISCUSSION

By coupling high-density EEG with the definition of functional ROIs obtained from fMRI (Cottereau et al. 2012a, see also Pitzalis et al. 2013 for a similar approach), we were able to characterize the dynamics of the cortical responses to 2D and 3D motion within distinct visual ROIs. Our stimuli were monocularly identical and only differed in their interocular phase difference (see Fig. 1). We found both amplitude and phase effect in all our functionally defined ROIs and also in parietal regions that were anatomically defined. An analysis of the SNRs showed that, compared with the responses to lateral motion, responses to MID are more asymmetric (i.e., they have bigger odd harmonics and weaker even harmonics, see Figs. 4 and 8). The same result was found for all the disparity pedestals. In addition, the SNR of the odd harmonic responses to MID is affected by the disparity offsets (see Figs. 6 and 9). This modulation is consistent with the absolute disparity-tuning curves that we characterized in a previous study (Cottereau et al. 2011) where asymmetries existed between the population responses to 4 arcmin crossed and uncrossed, but also between the responses to 2 and 10 arcmin uncrossed or between the responses to 6 and 14 arcmin uncrossed (see also the *Effects of the disparity offset from the fixation plane* section). In addition to these asymmetries caused by the cortical responses to absolute disparity, our odd harmonics SNRs might also reflect responses from neural populations selective to higher-order disparity mechanisms. Indeed, our MID stimulus contains relative disparities between the moving bars and the static background that remains in the fixation plan. Among our ROIs, V3A has specific responses to relative disparity (Backus et al. 2001; Cottereau et al. 2011; Tsao et al. 2003) that remain strongly dependent on the absolute disparity responses (Cottereau et al. 2012). These responses should preserve the asymmetries present in the disparity tuning curves. It is therefore possible that the difference we measured between the amplitudes associated to MID and lateral motion at odd harmonics are caused by the specific disparity values used in our experimental protocol.

At least two alternative hypotheses involving more general mechanisms should, however, be considered. First, disparity-defined objects can be seen in our MID stimulus when the bars are in front of the static reference. In the ventral pathway, the LOC has specific responses to disparity-defined objects (Cottereau et al. 2011; Gilaie-Dotan et al. 2002). Several regions within our superior parietal ROI have the same properties: the ventral portion of the intraparietal suclus and the dorsal and medial part of the intraparietal sulcus (see Durand et al. 2009). Our odd harmonics could also reflect asymmetries between forward and backward motion. To our knowledge, this hypothesis has never been tested for 3D motion defined by interocular phase differences. Using nonstereoscopic presentations, several studies have suggested that the responses to inward optic flow (looming) were stronger than the responses to "receding" optic flow in the occipital cortex (Lamberty et al. 2008; Wunderlich et al. 2002).

The SNR for lateral motion is around 6 dB (i.e., 2 times in linear scale) larger than that obtained for MID within each of our ROIs, regardless of the pedestal value. The strength of this effect suggests that it reflects a general difference between the processing of 2D and 3D motion. This amplitude suppression for MID is consistent with the fact that lateral motion is far more detectable than stereo motion (Harris et al. 1998; Tyler 1971; Tyler and Foley 1974; Westheimer 1990). Interestingly, this effect already exists in the V1 ROI, suggesting a suppression caused by the combination of the two monocular signals.

We also found consistent phase differences between lateral motion and MID for the three pedestals (see Table 1). Our results reveal consistent lags for MID. This difference in the temporal characteristics of lateral motion and MID, combined with the smaller even harmonic responses for MID, may contribute to the poorer psychophysical sensitivity to rapid oscillations in depth originally found by Regan and Beverley (1973a, 1973b). There is other indirect evidence that MID processing is slow compared with lateral motion. Voluntary convergence has a longer latency (~160 ms) and a worse response to sinusoidal motion along the *z*-axis (Rashbass and Westheimer 1961), compared with pursuit (velocity driven), which has a short latency (~100 ms) and good response to sinusoidal motion along the *x*-axis. In our study, time-lags are present as early as the V1 ROI and then increase in the extrastriate ROIs, suggesting additional processing for MID within these higher visual ROIs. On average, the longest lags (mainly in the V3A ROI but also in ROIs V4 and hMT+) correspond to a delay for MID of as much as 45 ms (these lags increase to 55 ms in our superior parietal ROI), a value close to the 60-ms latency difference between convergence and pursuit described above.

Using a novel functional connectivity analysis, we found response covariations between ROIs V1 and LOC during both MID and lateral motion. The LOC is involved in many aspects of object processing (Kourtzi and Kanwisher 2002). More particularly, it combines stereo and motion cues for object segmentation (Vinberg and Grill-Spector 2008). The moving bars in our stimuli were surrounded by a static background and were therefore seen as moving relative to this background. The connection between ROIs V1 and LOC is thus consistent with the LOC, integrating both motion and stereo cues from early visual areas to segment the bars from their background.

We also found strong connections between the V3A and hMT+ ROIs during MID. Importantly, these connections were statistically significant for all the disparity pedestals and are therefore probably independent of the specific disparity values used in our experiment. Recent fMRI studies have demonstrated that both areas hMT+ and V3A are highly responsive to various aspects of MID (Rokers et al. 2009). In our previous work, we emphasized that the V3A ROI responded strongly to a central disk alternating between disparities (Cottereau et al. 2012b, 2012c). Our connectivity analysis extends these results by suggesting that both the hMT+ and V3A ROIs are con-

nected within a cortical network specifically devoted to the processing of MID.

As described in the Introduction, MID can be perceived via two different cues: the interocular velocity difference (IOVD) and the CDOT. Our stimuli contained information about both CDOT and IOVD, so either or both cues might have generated our measured responses to MID. There are several considerations suggesting that our responses were dominated by CDOT. First, we found an effect of the disparity pedestals on the SNR at odd harmonics (Fig. 6). The pedestals modify the disparity information but leave the IOVD unchanged, which implies that at least some portion of our responses at odd harmonics was driven by disparity selective cells. In a previous study where we used dynamic random dot stimuli that selectively isolated disparity (Cottereau et al. 2011), we showed that the responses to CDOT always contained both odd and even harmonics, with the SNRs at even harmonics being stronger than those at odd harmonics (see Figs. 3 and 4 in Cottereau et al. 2011). Thus the even harmonics also contained some disparity-related components. Second, in a recent study, Czuba et al. (2010) compared MID sensitivity for a full cue condition (both cues present) to stimuli that selectively stimulated either disparity alone or interocular velocity alone. They showed that for the central stimulation (stimuli falling within the central 14°) and the slow speeds ($\sim 0.3° \cdot s^{-1} \cdot eye^{-1}$) used in our study, sensitivity for disparity stimuli matched performance for the full cue condition and was substantially better than sensitivity for IOVD stimuli. Finally, the lag difference that we found between the responses to lateral motion and MID is consistent with the results obtained by Ponce and collaborators (2008) in a study where they combined single-cell recordings with deactivation by cooling. They showed that motion responses follow a direct pathway that goes directly from V1 to MT, while disparity responses follow an indirect pathway passing through areas V2 and V3. The additional lags for MID that we observe in higher visual areas could be the signature of this indirect pathway.

Although these considerations suggest a strong contribution of disparity-selective populations to our results, we cannot rule out that some portion of our responses were also generated by IOVD-selective populations (including neurons responsive to the IOVD difference between our bars and the static reference). It would be interesting to learn if the phase differences we observed in our study diminish for faster and more eccentric stimuli where MID perception is more dependent on IOVD (Czuba et al. 2010). Because IOVD is based on the monocular motion elicited in each of the two eyes, the timing of responses dominated by IOVD might be closer to those of lateral motion.

## ACKNOWLEDGMENTS

The authors thank Doug Taylor for help in the design of the stimuli used in this study.

## GRANTS

This work was supported by National Eye Institute Grants R01 EY-018875, the Smith-Kettlewell Eye Research Institute, and a Walt and Lilly Disney Amblyopia Research Award from Research to Prevent Blindness.

## DISCLOSURES

No conflicts of interest, financial or otherwise, are declared by the author(s).

## AUTHOR CONTRIBUTIONS

Author contributions: B.R.C., S.P.M., and A.M.N. conception and design of research; B.R.C. and S.P.M. performed experiments; B.R.C. analyzed data; B.R.C., S.P.M., and A.M.N. interpreted results of experiments; B.R.C. prepared figures; B.R.C. drafted manuscript; B.R.C., S.P.M., and A.M.N. edited and revised manuscript; B.R.C., S.P.M., and A.M.N. approved final version of manuscript.

## REFERENCES

**Appelbaum LG, Wade AR, Vildavski VY, Pettet MW, Norcia AM.** Cue-invariant networks for figure and background processing in human visual cortex. *J Neurosci* 26: 11695–11708, 2006.

**Backus BT, Fleet DJ, Parker AJ, Heeger DJ.** Human cortical activity correlates with stereoscopic depth perception. *J Neurophysiol* 86: 2054–2058, 2001.

**Baillet SM, Mosher JC, Leahy RM.** Electromagnetic brain mapping. *IEEE Signal Process Mag* 18: 14–30, 2001.

**Berens P.** CircStat: a MATLAB toolbox for circular statistics. *J Stat Softw* 31: 1–21, 2009.

**Berens P, Keliris GA, Ecker AS, Logothetis NK, Tolias AS.** Comparing the feature selectivity of the gamma-band of the local field potential and the underlying spiking activity in primate visual cortex. *Front Syst Neurosci* 2: 2, 2008.

**Beverley KI, Regan D.** The relation between discrimination and sensitivity in the perception of motion in depth. *J Physiol* 249: 387–398, 1975.

**Brewer AA, Liu J, Wade AR, Wandell BA.** Visual fields maps and stimulus selectivity in human ventral occipital cortex. *Nat Neurosci* 8: 1102–1109, 2005.

**Cottereau BR, Ales JM, Norcia AM.** Increasing the accuracy of electromagnetic inverses using functional area source correlation constraints. *Hum Brain Mapp* 33: 2694–2713, 2012a.

**Cottereau BR, McKee SP, Ales JM, Norcia AM.** Disparity tuning of the population responses in the human visual cortex: an EEG source imaging study. *J Neurosci* 31: 954–965, 2011.

**Cottereau BR, McKee SP, Ales JM, Norcia AM.** Disparity-specific spatial interactions: Evidence from EEG source imaging. *J Neurosci* 32: 826–840, 2012b.

**Cottereau BR, McKee SP, Norcia AM.** Bridging the gap: global disparity processing in the human visual cortex. *J Neurophysiol* 107: 2421–2429, 2012c.

**Cumming BG, Parker AJ.** Binocular mechanisms for detecting motion-in-depth. *Vision Res* 34: 483–495, 1994.

**Czuba TB, Rokers B, Huk AC, Cormack LK.** Speed and eccentricity tuning reveal a central role for the velocity-based cue to 3D visual motion. *J Neurophysiol* 104: 2886–2899, 2010.

**Desikan RS, Segonne F, Fischl B, Quinn BT, Dickerson BC, Blacker D, Buckner RL, Dale AM, Maguire RP, Hyman BT, Albert MS, Killiany RJ.** An automated labeling system for subdividing the human cerebral cortex on MRI scans into gyral based regions of interest. *Neuroimage* 31: 968–980, 2006.

**Durand JB, Peeters R, Norman JF, Todd JT, Orban GA.** Parietal regions processing visual 3D shape extracted from disparity. *Neuroimage* 46: 1114–1126, 2009.

**Fischl B, Sereno MI, Tootell RB, Dale AM.** High-resolution intersubject averaging and a coordinate system for the cortical surface. *Hum Brain Mapp* 8: 272–284, 1999.

**Fisher NI.** *Statistical Analysis Of Circular Data*. Cambridge, UK: Cambridge University Press, 1995.

**Gilaie-Dotan S, Ullman S, Kushnir T, Malach R.** Shape-selective stereo processing in human object-related visual areas. *Hum Brain Mapp* 15: 67–79, 2002.

**Hämäläinen M, Hari R, Ilmoniemi R, Knuutila J, Lounasmaa O.** Magnetoencephalography: theory, instrumentation and applications to the non-invasive study of human brain function. *Rev Mod Phys* 65: 413–497, 1993.

**Hämäläinen MS, Sarvas J.** Relistic conductivity geometry model of the human head for interpretation of neuromagnetic data. *IEEE Trans Biomed Eng* 36: 165–171, 1989.

**Harris JM, McKee SP, Watamaniuk SNJ.** Visual search for motion in depth: stereomotion does not "pop-out" from disparity noise. *Nat Neurosci* 1: 165–168, 1998.

**Harrison D, Kanji GK.** The development of analysis of variance for circular data. *J Appl Stat* 15: 197, 1988.

**Huk AC, Heeger DJ.** Pattern-motion responses in human visual cortex. *Nat Neurosci* 5: 72–75, 2002.

**Kourtzi Z, Kanwisher N.** Cortical regions involved in perceiving object shape. *J Neurosci* 20: 3310–3318, 2002.

**Lachaux JP, Rodriguez E, Martinerie J, Varela FJ.** Measuring phase synchrony in brain signals. *Hum Brain Mapp* 8: 194–208, 1999.

**Lages M, Heron S.** On the inverse problem of binocular 3D motion perception. *PLoS Comput Biol* 6: e1000999, 2010.

**Lamberty K, Gobbelé R, Schoth F, Buchner H, Waberski TD.** The temporal pattern of motion in depth perception derived from ERPs in humans. *Neurosci Lett* 439: 198–202, 2008.

**Nefs HT, O'Hare L, Harris JM.** Two independent mechanisms for motion-in-depth perception: evidence from individual differences. *Front Psychol* 1: 155, 2010.

**Nienborg H, Bridge H, Parker AJ, Cumming BG.** Neural computation of disparity in V1 limits temporal resolution for detecting disparity modulation. *J Neurosci* 25: 10207–10219, 2005.

**Norcia AM, Tyler CW.** Temporal frequency limits for stereoscopic apparent motion processes. *Vision Res* 24: 395–401, 1984.

**Pascual-Marqui R, Michel C, Lehman D.** Low-resolution electromagnetic tomography: a new method for localizing electrical activity in the brain. *Int J Psychophysiol* 18: 49–65, 1994.

**Pitzalis S, Sdoia S, Bultrini A, Committeri G, Di Russo F, F, Fattori P, Galletti C, Galati G.** Selectivity to translational egomotion in human brain motion areas. *PLoS One* 8: e60241, 2013.

**Ponce CR, Lomber SG, Born RT.** Integrating motion and depth via parallel pathways. *Nat Neurosci* 11: 216–223, 2008.

**Rashbass C, Westheimer G.** Disjunctive eye movements. *J Physiol* 159: 339–360, 1961.

**Regan D, Beverley KI.** Some dynamic features of depth perception. *Vision Res* 13: 2369–2379, 1973a.

**Regan D, Beverley KI.** The dissociation of sideways movements from movements in depth: psychophysics. *Vision Res* 13: 2403–2415, 1973b.

**Rokers B, Cormack LK, Huk AC.** Disparity-and velocity-based signals for three-dimensional motion perception in human MT+. *Nat Neurosci* 12: 1050–1055, 2009.

**Smith SM.** Fast robust automated brain extraction. *Hum Brain Mapp* 17: 143–155, 2002.

**Smith SM, Jenkinson M, Woolrich MW, Beckmann CF, Behrens TE, Johansen-Berg H.** Advances in functional and structural MR image analysis and implementation as FSL. *Neuroimage* 23, *Suppl* 1: 208–219, 2004.

**Stephens MA.** Multi-sample tests for the fisher distribution for directions. *Biometrika* 56: 169–181, 1969.

**Tolias AS, Ecker AS, Siapas AG, Hoenselaar A, Keliris GA, Logothetis NK.** Recording chronically from the same neurons in awake behaving primates. *J Neurophysiol* 98: 3780–3790, 2007.

**Tsao DY, Vanduffel W, Sasaki Y, Fize D, Knutsen TA, Mandeville JB, Wald LL, Dale AM, Rosen BR, Van Essen DC, Livingstone MS, Orban GA, Tootell RBH.** Stereopsis activates V3A and caudal intraparietal areas in macaques and humans. *Neuron* 39: 555–568, 2003.

**Tyler CW.** Stereoscopic depth movement: two eyes less sensitive than one. *Science* 174: 958–961, 1971.

**Tyler CW, Foley JM.** Stereomovement suppression for transient disparity changes. *Perception* 3: 287–296, 1974.

**Vialatte FB, Maurice M, Dauwels J, Cichocki A.** Steady-state visually evoked potentials: focus on essential paradigms and future perspectives. *Prog Neurobiol* 90: 418–438, 2010.

**Vinberg J, Grill-Spector K.** Representation of shapes, edges, and surfaces across multiple cues in the human visual cortex. *J Neurophysiol* 99: 1380–1393, 2008.

**Vinck M, Oostenveld R, Van WM, Battaglia F, Pennartz CM.** An improved index of phase-synchronization for electrophysiological data in the presence of volume-conduction, noise and sample-size bias. *Neuroimage* 55: 1548–1565, 2011.

**Wade AR, Brewer AA, Rieger JW, Wandell BA.** Functional measurements of human ventral occipital cortex: retinotopy and color. *Philos Trans R Soc Lond B Biol Sci* 357: 963–973, 2002.

**Watson GS, Williams EJ.** On the construction of significance tests on the circle and the sphere. *Biometrika* 43: 344–352, 1956.

**Westheimer G.** Detection of disparity motion by the human observer. *Optom Vis Sci* 67: 627–630, 1990.

**Wunderlich G, Marshall JC, Amunts K, Weiss PH, Mohlberg H, Zafirirs O, Zilles K, Fink GR.** The importance of seeing it coming: a functional magnetic resonance study of motion-in-depth towards the human observer. *Neuroscience* 112: 535–540, 2002.

**Yeo BT, Sabuncu MR, Vercauteren T, Ayache N, Fischl B, Golland P.** Spherical demons: fast diffeomorphic landmark-free surface registration. *IEEE Trans Med Imaging* 29: 650–668, 2010a.

**Yeo BT, Sabuncu MR, Vercauteren T, Holt DJ, Amunts K, Zilles K, Golland P, Fischl B.** Learning task-optimal registration cost functions for localizing cytoarchitecture and function in the cerebral cortex. *IEEE Trans Med Imaging* 29: 1424–1441, 2010b.

**Zar JH.** *Biostatistical Analysis* (4th Ed.). New York: Prentice Hall, 1999.